Excitation of toroidal Alfvén eigenmodes with counter-current NBI in the TCV tokamak

M. Vallar[1],* ⓘ**, M. Dreval[2,3], M. Garcia-Munoz[4]** ⓘ**, S. Sharapov[5]** ⓘ**, J. Poley[1], A. N. Karpushov[1], P. Lauber[6], S. Mazzi[1], L. Porte[1] and the TCV Team[a]**

[1] Ecole Polytechnique Fédérale de Lausanne (EPFL), Swiss Plasma Center (SPC), CH-1015 Lausanne, Switzerland
[2] Institute of Plasma Physics, National Science Center, Kharkov Institute of Physics and Technology, 61108 Kharkov, Ukraine
[3] V.N. Karazin Kharkiv National University, Kharkiv, Ukraine
[4] Department of Atomic, Molecular and Nuclear Physics, University of Seville, Seville, Spain
[5] CCFE, Culham Science Centre, Abingdon, United Kingdom of Great Britain and Northern Ireland
[6] Max-Planck Institute for Plasma Physics, Garching, Germany

E-mail: matteo.vallar@epfl.ch

CrossMark

Abstract

In Tokamak á Configuration Variable (TCV), unstable modes excited by resonant interaction between the shear Alfvèn waves in continuum gaps and energetic particles have been observed in scenarios with neutral beam injection (NBI). TCV is a middle-size device ($R_0/a = 0.88/0.25$) equipped with a 1 MW, 25 keV tangential neutral beam injector. In this paper the phenomenology of modes excited with on-axis NBI is presented. The Alfvènic nature of the modes has been confirmed investigating their sensitivity against plasma parameters such as NBI energy, toroidal magnetic field, and cross-checking with the predictions from linear kinetic stability code. The mode radial profile is estimated using electron cyclotron emission measurement and agrees well with modelling results. In addition, the fast particle distribution function has been modelled using TRANSP/NUBEAM code. Even with counter-current NBI (leading to higher losses), the drive from the resonant particles is sufficient for the mode excitation. An ad-hoc additional diffusion model allows to estimate the fast particle transport, modifying the fast particle gradient at the mode location and matching the neutron rates.

Keywords: tokamak, fast particles, TCV, TAE

(Some figures may appear in colour only in the online journal)

1. Introduction

Magnetohydrodynamic (MHD) modes excited by energetic particles are a challenge for future fusion reactors, such as ITER, since they can cause degradation of α particles' confinement, plasma heating, and create hot-spots on the plasma facing components. Thus, the study of such MHD modes and their suppression is of fundamental importance for present and future fusion devices.

Among the possible weakly damped Alfvén eigenmodes we find the Toroidal Alfvèn Eigenmodes (TAEs) [1, 2], lying in the gap of the shear Alfvèn waves (SAWs) continuum caused by the toroidal geometry of tokamak devices. Additional gaps can be opened due to the plasma poloidal shape ellipticity and non-circularity, exciting respectively the Elliptic Alfvén Eigenmodes and Non-circular Alfvén Eigenmodes. The gradients in real and velocity space of the fast particles can drive modes in the gap through the fundamental wave-particle resonant mechanism, causing perturbations of the electromagnetic fields. Such perturbations can be detected by the magnetic sensors and can induce large fast-ion transport.

The Tokamak á Configuration Variable (TCV) [3]) is a flexible device equipped with two tangential neutral beam (NB) injectors [4], both with a nominal injected power of $\geqslant 1$ MW. The study on the fast ion population injected by such beams and on the interaction with MHD modes has been explored in [5–7]. TCV is also equipped with electron cyclotron emission (ECE) diagnostic and short pulse reflectometry [8], which allow to measure the fine fluctuations of electron temperature and density and thus reconstruct the MHD mode spatial structure. TCV's capability to explore non-conventional plasma shapes (such as negative triangularity [9]) and its high electron cyclotron resonance heating (ECH) power available ($\leqslant 3.5$ MW) makes it an attractive device where energetic particle modes can be studied and their suppression achieved. The common way to suppress TAEs is through localized current drive, which modifies the local SAW continuum structure and increases the continuum damping by closing the gap [10, 11].

In this work, interpretation of the MHD activity induced by energetic particles is done. The MHD activity is observed experimentally in the fluctuations on the magnetic field and in the ECE. The additional fast ion transport can be inferred from the neutron rate. The experimental data are used as input for linear MHD stability tools and fast ion transport codes in order to infer the type of MHD activity and the additional fast ion transport related to the magnetic mode.

The paper is structured as follows. In section 2 the experimental scenario is presented. In section 3 the identification of the modes magnetic structure is presented. In section 4, the linear stability is analysed using the LIGKA code. In the end, the fast particle population is analysed with the TRANSP/NUBEAM codes in section 5 before drawing the conclusions.

2. Experimental scenario overview

TCV is a medium-size device ($R_0/a = 0.88$ m/0.25 m) capable of flexible plasma shaping due to 16 independent poloidal field coils and an over-sized vacuum chamber. Available heating systems include ERCH and two tangential NBIs with 1 MW–1.3 MW in deuterium and energies $\leqslant 28$ keV and $\leqslant 42$ keV [4, 12, 13] arranged anti-collinearly at the TCV midplane (see figure 1(*a*)). The width of the beam (computed as the size with 1/e intensity of the interpolated beam footprint on the calorimeter) is 21.6 cm $\times$ 9.4 cm at the port entrance (horizontal $\times$ vertical).

TCV is equipped with a large set of diagnostics. Electron density and temperature are measured by a Thomson scattering diagnostic, while the ion temperature and toroidal velocity by charge exchange recombination spectroscopy. Interferometry is used to measure the line-averaged electron density. The amplitude of the magnetic field perturbation is measured from the standard pick-up coils and LTCC-3D diagnostic [14, 15]. The latter has a maximum resolvable frequency of 2 MHz, enabling the reconstruction of the detected modes up to 1 MHz, and thereby the detection of changes in the continuum gaps induced by, e.g. the triangularity modifications.

The TCV plasma shot chosen for this analysis (#73116) features counter-current injection from the so-called NB1 (which means I_p and B_0 with positive sign, counter-clockwise from above, see figure 1(*a*)). The plasma current was kept at 120 kA and the magnetic field is changed between 1.3 T and 1.42 T throughout the pulse. NB1 power is scanned up to 1.3 MW. The plasma is in positive triangularity, as figure 1(*b*) shows.

The electron density on-axis is around 5×10^{19} m^{-3}, the on-axis ion and electron temperature is around 0.4 keV, as figure 2 shows.

This scenario is significantly different with respect to the one published in [16]. In that case, the aim was to minimise the energetic particles collisionality and have a good balance in the fast particle content. To do so, the injection was both co-current and off-axis (with $z_0 \sim 12$ cm) to aim on a plasma region where the collisionality (i.e. the density) was low. Furthermore, the plasma was heated with ECRH in order to reduce the collisionality by increasing T_e. The modes observed in that case had a different structure with respect to the ones observed here (see section 4 for further details). In the case studied in this work, no electron cyclotron heating is needed, the plasma is centred at $z = 5$ cm and NBI is injected counter-current. By doing so, we are reducing the fast particle content (avoiding a too high fast particle fraction, which could produce unwanted MHD modes). In addition the configuration with $z_0 < 5$ cm and no ECHR allows a larger flexibility in the application of control techniques for TAEs, such as localized current drive [10, 11].

3. Experimental mode identification

TCV shot #73116 features some relevant MHD activity, which can be directly correlated to both NB1 fast particle energy and
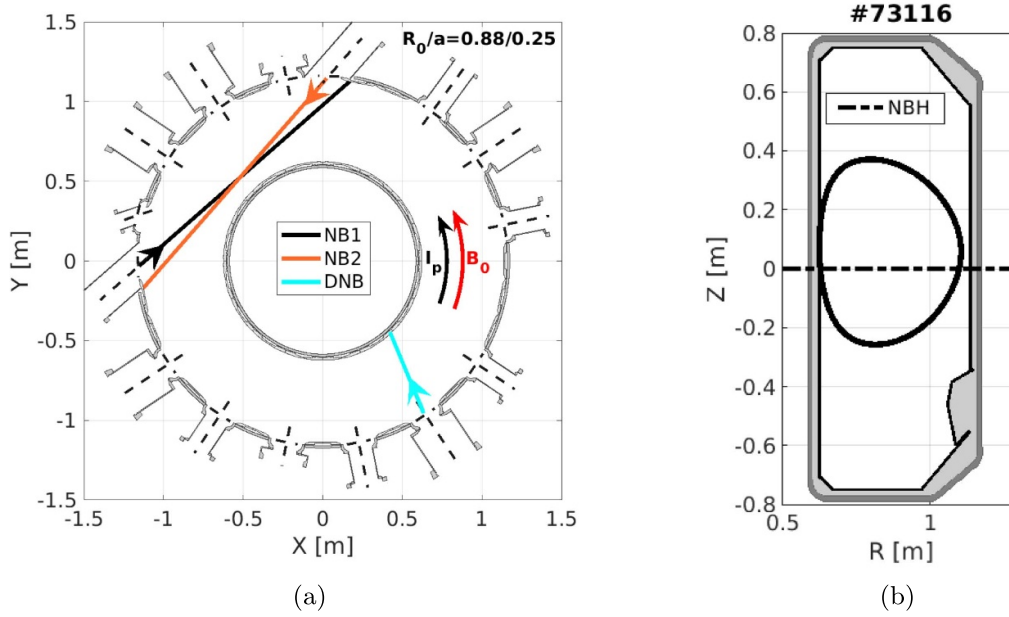
(a)

(b)

Figure 1. (*a*) Top view of TCV device. Black (blue) solid line is the approximate NB1 (NB2) injection line. The Diagnostic NB is shown in cyan and labelled as DNB. (*b*) Sketch of the shape of the plasma analysed in this study. Dotted line at $z = 0$ m is the injection geometry NB1 and NB2, corresponding to the midplane.
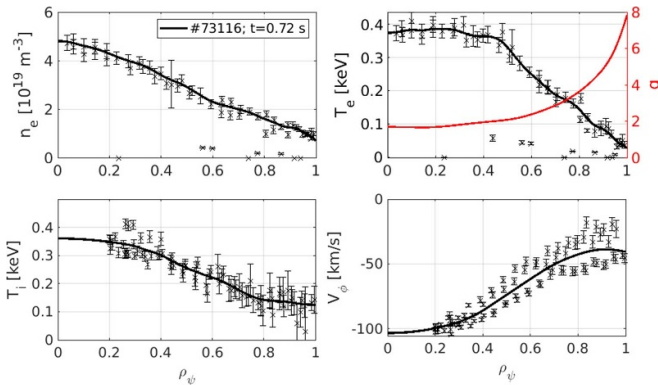

Figure 2. Profiles of the relevant quantities for shot 73 116 at $t = 0.72$ s. Electron density (n_e) and electron temperature (T_e) are reconstructed from Thomson scattering data. q profile is reconstructed through kinetic equilibrium reconstruction. Ion temperature (T_i) and toroidal rotation (V_ϕ) are reconstructed from charge exchange recombination spectroscopy.

B_0. In figure 3(*a*), the MHD activity is visible in a spectrogram representing the whole plasma discharge. The data come from the variation of poloidal magnetic field measured with LTCC-3D diagnostic. As illustrated by the white line in the bottom of figure 3(*a*), the NB1 power is smoothly varied in the first phase ($t \lesssim 0.8$ s) of the shot to evaluate the relation between the fast particle energy and the presence of any MHD signal. It is needed to change the power because that's the only way to modify NB1 fast particle energy [12]. It can be seen that the MHD activity at 100 kHz appears only for a given fast particle energy (which is larger than 24.5 keV at 0.9 MW). On the other hand, the modes at higher frequency (180 kHz) appear only when the maximum beam power and energy is reached,

i.e. respectively at 1.3 MW and 26 keV (vertical orange line in the figure).

The mode dependence on the toroidal magnetic field is shown in the latter part of the shot ($t \gtrsim 1$ s), where the beam power is kept constant but B_0 is increased from 1.3 T to 1.42 T. The frequency of the modes increases linearly with the increasing magnetic field.

An interesting feature can be seen zooming on a smaller time window, as reported in figure 3(*b*). The MHD modes (either at 100 kHz and 180 kHz) appear to be intermittent with a characteristic time of $\sim$1 ms. Adding the experimentally measured neutron rate waveform to the plot (in arbitrary units, cyan light), we can see that the neutron rate from beam-target DD fusion reactions oscillates with a similar characteristic time period.

In order to identify the mode frequency, the power spectral density (PDS) of the poloidal magnetic field variation at the wall at the selected time instant $t = 0.72$ s is shown in figure 4(*a*). The two dominant modes considered for this work (100 kHz and 180 kHz) present toroidal mode number $n = 1$. A weaker unstable mode detected at 285 kHz has $n = 0$ toroidal mode number. Preliminary studies suggest that this latter mode could be excited by a bump-on tail in the fast-ion distribution caused by the ejection of fast ions induced by the $n = 1$ modes. The $n = 0$ mode will not be taken into consideration for this work.

Averaging the neutron rates may provide a clear correlation between the modes amplitude and the neutrons emitted from the plasma. In figure 4(*b*) the results of this analysis are shown. Every data point is the average (over multiple cycles) of the neutron rate at a normalized time distance from a mode amplitude peak. The black (red) dots are related to the 100 kHz (180 kHz) mode. For the black case, the maximum of
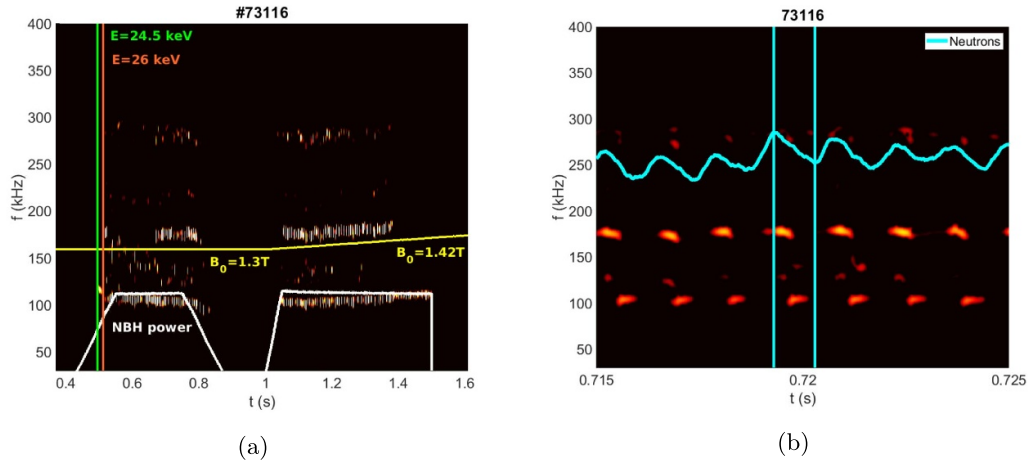
Figure 3. (*a*) Spectrogram of the poloidal magnetic field signal over the entire plasma shot time window. In addition, the beam power trace (white), the toroidal magnetic field (yellow), and the points where the beam energy reaches a given value (orange and green) are shown. (*b*) A zoom of the spectrogram on a smaller time window, with the cyan oscillating curve indicating the neutron rate signal in time, and the vertical cyan lines indicating the maximum and minimum of the neutron rates for a cycle.
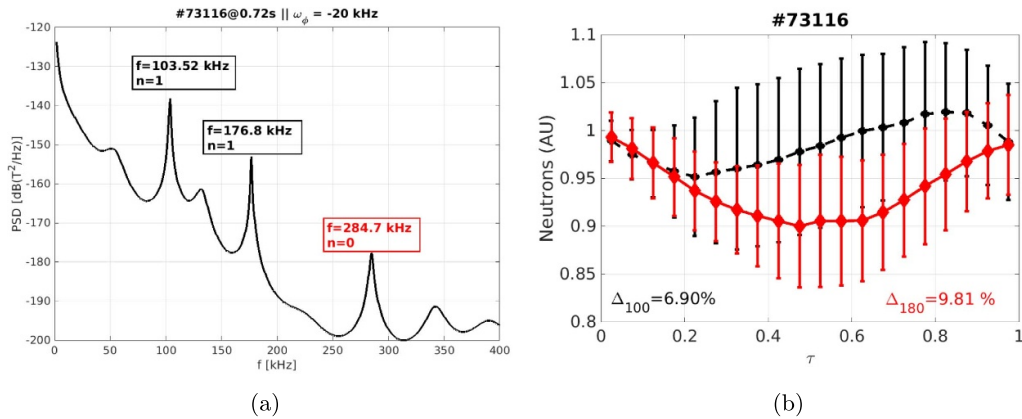

Figure 4. (*a*) Power spectral density and toroidal mode number of the detected modes, at $t = 0.72\,\text{s}$ (*b*) averaging of the neutron rates with respect to the maximum amplitude of 100 kHz mode (black) and 180 kHz mode (red). The *x*-axis represents the time normalized with respect to the time instant at which the mode amplitude is maximal. The leftmost point ($\tau = 0$) is the time of the cycle maximum, while the rightmost ($\tau = 1$) is the maximum of the next cycle. The *y*-axis is normalized such that at $\tau = 0$ the neutron rate is 1 for each cycle.

the neutron rates is not corresponding to the maximum of the peak amplitude. Indeed, for the red case, the maximum corresponds to the maximum amplitude. The drop in neutron rate is slightly larger (in percentage) for the mode at 180 kHz, reaching roughly 10% with respect to 7% for the 100 kHz mode. Therefore from this analysis, it can be said that the total neutron rate is likely more correlated and more affected by the 180 kHz mode.

Given the observations above, the time-scale ($\tau \sim 1\,\text{ms}$) of the mode dynamics suggests that the main actor at play is the fast ion population, and not the bulk plasma. The mode at higher frequency could lie inner in the plasma core (as expected for TAEs), in a region where the fast ion distribution exchanges energy with it. Therefore, fast ions are expelled from such inner region due to the large-amplitude magnetic perturbations induced by the instability, and the neutron rate decreases accordingly. This radial fast-particle transport populates the more outwards regions, where the wave-particle

resonant interaction between the lower frequency mode and the fast ions is more favourable. At the moment when the resonant fast ion population is sufficiently depleted, the mode disappears and the neutron rate increases with the piling up of energetic particles, triggering the same cycle again. This interpretation is supported by numerical modelling in the following sections.

4. Linear MHD stability

The linear stability at $t = 0.72\,\text{s}$ is investigated by means of the linear gyrokinetic eigenvalue solver LIGKA [17] and the linear ideal MHD code MISHKA [18].

In the current work, only the frequency range of the TAE is considered. The spatial location of a TAE depends on its toroidal (n) and poloidal (m) mode numbers, and the following relation must be satisfied
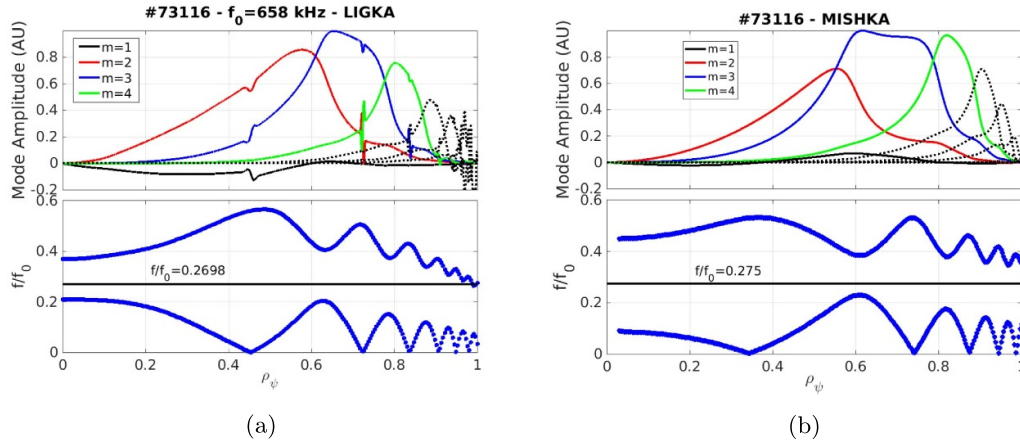
Figure 5. Shot #73116, upper panel: mode structure for the gap relative to $m = (2, 3)$. Colour codes in the legend. Lower panel: SAW continuum (in blue) with the modelled frequency (black line). (*a*) LIGKA code (*b*) MISHKA code.

$$q = \frac{m + 1/2}{n}. \tag{1}$$

In the following, $n = 1$ and $m = 2, 3$ ($q = 5/2, 7/2$) values are taken into account. In figure 5 the mode structure (top pane) and the SAW continuum (bottom pane) are shown for LIGKA (figure 5(*a*)) and MISHKA (figure 5(*b*)). The two codes are in good agreement, so only the LIGKA case will be discussed in the following. This confirms the robustness of the input data and the physics included in the two codes. The coloured curves in figure 5(*a*) represent the mode peaking at $q = 5/2$, with its harmonics ($\rho_\psi \cong 0.6$, in radial coordinate, where $\rho_\psi = \sqrt{\psi_{\text{pol. norm.}}}$ is the normalized poloidal magnetic flux coordinate). The corresponding frequency is $\omega_{2,3} = 0.2698 \times f_0 \sim 177\,\text{kHz}$, being f_0 the on-axis Alfvén velocity, which is in quite good agreement with the frequency observed experimentally (see figures 3(*a*) or 4). This mode features a global structure, extending all over the whole plasma radius.

The SAW continuum for $n = 1$ is shown in the lower panel in figure 5(*a*). The blue line represents the continuum structure computed considering only ideal MHD. The small ratio between the kinetic and the magnetic plasma pressure (β) does not modifies significantly the continuum, and it is not shown in the figure.

The modes located in the contiguous gap $q = 7/2$ ($\rho_\psi \cong 0.8$), due to the coupling of the poloidal mode numbers $m = 3, 4$ has a computed frequency of $\omega_{3,4} = 0.176 \times f_0 \sim 115\,\text{kHz}$, in good agreement with LTCC-3D magnetic measurement. From the LIGKA modelling, the low frequency mode crosses the continuum at around $\rho_\psi = 0.7$ and it is damped due to phase-mixing effects [19]. The radial localization of the low frequency TAE is thereby limited to the outer part of the plasma. As already noted, the least damped $n = 1$ TAEs detected using LIGKA code reproduce closely the experimental measurements. The slight difference (around 10%) in frequency can be explained by the errors in the toroidal velocity measurements and q-profile reconstruction. In this case, the toroidal rotation is $12.5\,\text{kHz} \pm 3\,\text{kHz}$.

In order to reconstruct the radial structure of the low frequency mode (the outer one), the ECE diagnostic [20] was employed in the TCV shot #73458, performed at very similar experimental conditions with respect to the previously discussed TCV shot #73116. Lower beam power (1 MW vs. 1.3 MW) was used in TCV shot #73458 to reduce beam fuelling and be far from the cutoff density. Six channels spacing the selected frequency range from 67.5958 GHz up to 68.2692 GHz are used for this diagnostic in TCV. Quite surprisingly, no correlation between contiguous acquisition channels is needed for the detection of such modes. This clearly indicates that the TAE-induced fluctuations in the electron temperature are well above the usual cut-off, and therefore that the detected TAEs are strongly unstable. Two different unstable modes are detected on the ECE radiometers, as the spectrogram in figure 6(*a*) and the PSD at a selected time point in figure 6(*b*) show. LIGKA modelling of shot #73458 confirms that the mode at 97 kHz is the $n = 1$, $m = 3, 4$ TAE, and the other at 195 kHz being its second harmonic. In fact, the $n = 1$, $m = 2, 3$ TAE frequency is computed to be localized around 120 kHz in this shot. This difference in simulated and detected frequency can be related to the omission of the toroidal rotation in the LIGKA modelling, which is not yet included in the code. The $n = 1$, $m = 2, 3$ TAE is not detected in shot #73458 because of the lower beam energy (needed to reduce the beam power) with respect to shot #73116. As already stated before and shown in figure 3(*a*), this prevents the $m = 2, 3$ TAE to be excited in shot #73458.

In order to further validate the results from the modelling, and additional analysis based on the comparison between the radial dependence of the ECE measured fluctuations of the temperature and the mode radial structure simulated with LIGKA is pursued. The results of this analysis are shown in figure 7(*a*). The radial locations of emission (with the horizontal errorbars) are calculated by TORAY code [21]. The
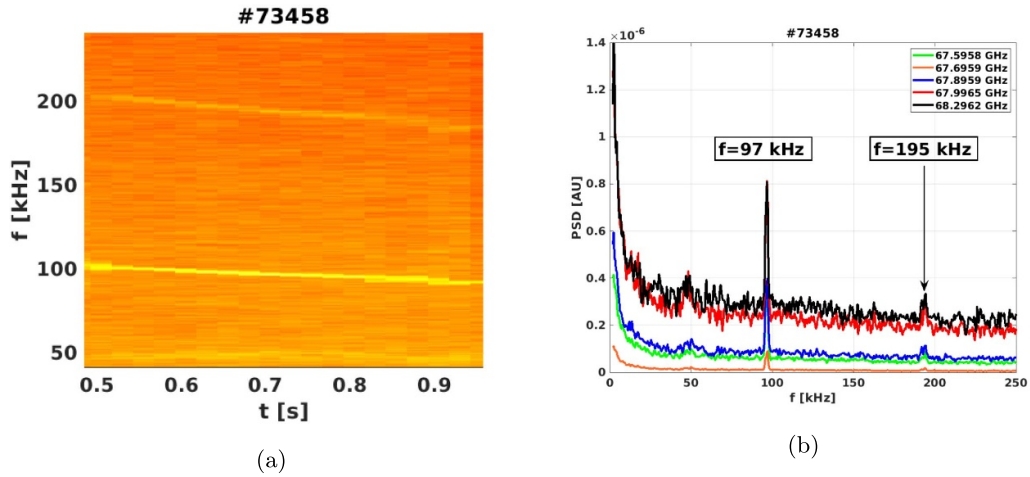
Figure 6. (*a*) ECE spectrogram for a selected channel. (*b*) The average power spectral density on a selected time window ($t = [0.5, 0.85]$ s), where the 97 kHz mode (and its harmonic at 195 kHz) is observed.
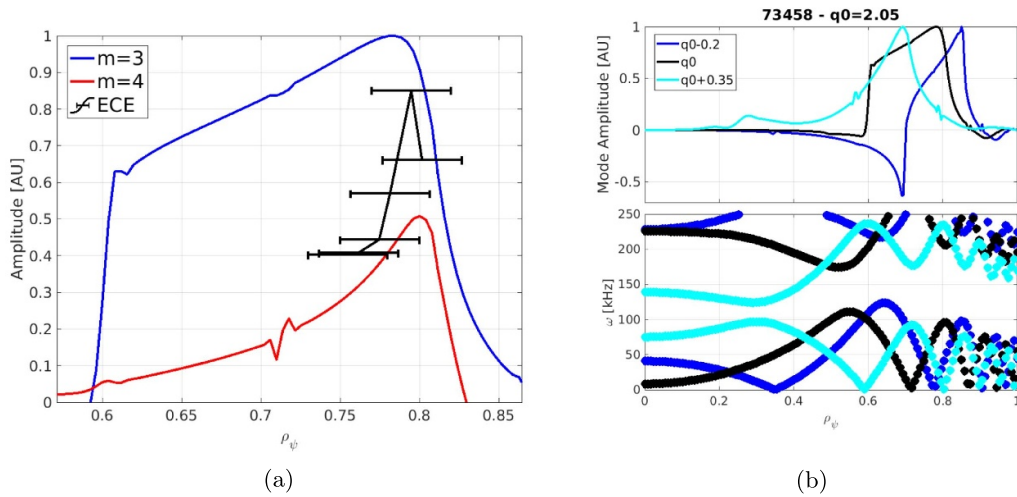

Figure 7. (*a*) The radial structure of the TAE modes ($n = 1, m = 3$) (in blue) and ($n = 1, m = 4$) (in red) are shown and compared to the reconstruction of the measurements of the six different ECE channels (black points with errorbars). The errorbars represent the error on the ECE location. (*b*) Sensitivity study on the q_0 value, which shows how a variation on the q_0 profile can modify the mode structure.

amplitude corresponds to the integral of the peak in the PSD, normalized to the total integral of the PSD. This allows to reconstruct the qualitative mode shape. Without normalization, a measurement of δT_e could be related to the variation δB induced by the mode, and this is left for future activities. It can be seen the noteworthy agreement between the ECE measured points and the radial structure of the mode simulated by LIGKA.

In figure 7(*b*) a sensitivity scan in the on-axis value of q ($q_0 = 2.05$) is shown for the mode m = 3. By slightly increasing the on-axis q value ($q_0 = 2.4$) it can be seen that the modes move slightly inwards and the crossing with the continuum moves largely inwards. Decreasing q_0 to 1.85, the mode moves outward, along with the crossing with the continuum. In this case, the mode is also much more peaked, as ECE measurements show. In addition, the continuum hills (on the lower side) originally at $\rho_\psi = 0.55$ and $\rho_\psi = 0.8$ have a larger distance in ω when reducing q, which further confirms how the

continuum is crossed more outwards. Such variation of the q profile reside well within the error in the *q*-axis reconstruction.

5. Interaction with fast particles

NB fast particles are the key ingredient to trigger the observed magnetic activity. However, several conditions need to be fulfilled for the interaction between fast particles and TAEs to be achieved [22]:

- $v_{\text{beam}} > v_{\text{A}}/3$, with v_{beam} the fast particle velocity and $v_{\text{A}} = \dfrac{B}{\sqrt{\mu_0 N_i}}$ the Alfvén velocity;
- minimization of the resonance condition $\Omega = \omega_{\text{EXP}} - n \cdot \omega_\phi + p \cdot \omega_\theta$, being ω_{EXP} the detected experimental frequency, *n* the measured toroidal mode number of the induced instability, ω_ϕ the toroidal frequency of the
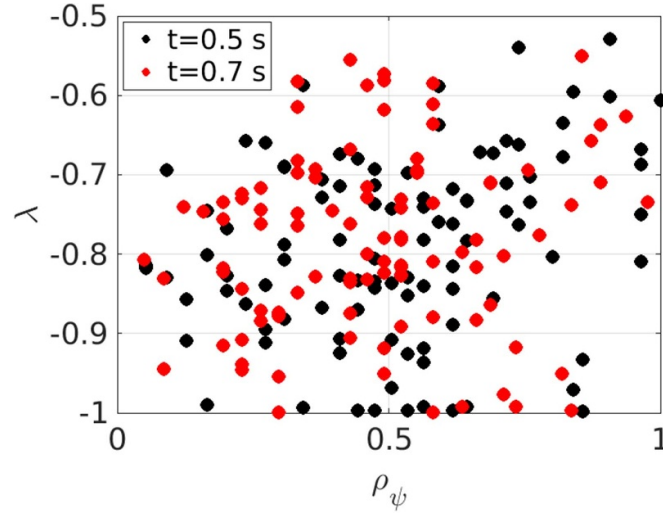
6

Figure 8. Initial (ρ_ψ, λ) phase-space of the NUBEAM markers at different time instants.
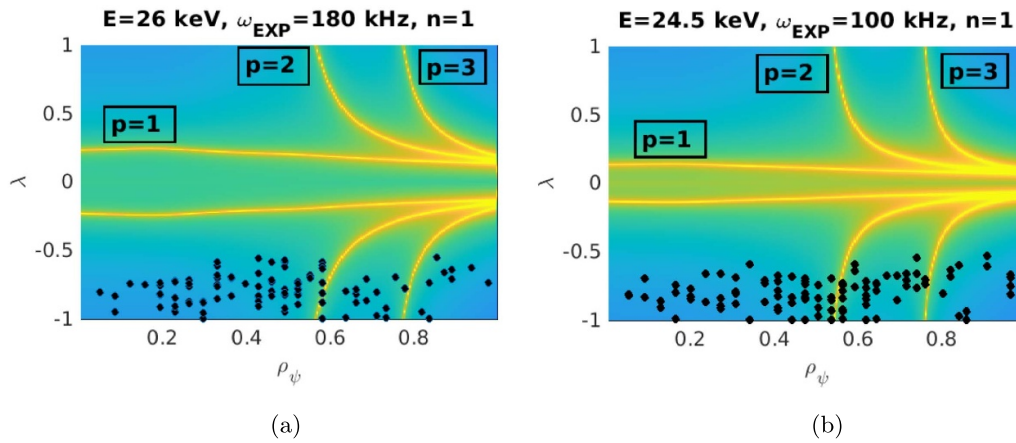

(a)

(b)

Figure 9. Values of the resonance condition Ω for $p = (1, 2, 3)$. Yellow means the resonance condition is minimized (*a*) Ω for $E = 26\,\mathrm{keV}$, for the frequency of the $(n, m) = (1, 2)$ TAE. (*b*) Ω for $E = 24.5\,\mathrm{keV}$, for the frequency of the $(n, m) = (1, 3)$ TAE. Black dots represent the initial phase-space location of the fast ion markers.

characteristic fast ion motion, p an integer, ω_θ the poloidal frequency of the fast ions;

- gradients of the fast ion distribution (in energy or space) exceed a threshold for wave-particle energy transfer to occur.

The value of v_{beam}/v_A is around 0.33, calculated for deuterium atoms injected, their energy of $\sim 26\,\mathrm{keV}$, the toroidal field of $B_0 = 1.3\,\mathrm{T}$ and the density of $3 \times 10^{19}\,\mathrm{m}^{-3}$. Therefore the first requirement of the list above is fulfilled, being the speed of the injected deuterons large enough to directly destabilize the TAEs through wave-particle resonant mechanism.

TRANSP/NUBEAM simulations are carried out in order to verify the remaining requirements. Those simulations are carried out retaining the realistic NB1 injection geometry. The fast particle initial population is shown in figure 8. The two separate time instants have two different energies (respectively 24.5 keV and 26 keV).

Starting from the magnetic equilibrium, the experimental frequency and the energy, $\Omega = \omega_{\mathrm{EXP}} - n \cdot \omega_\phi + p \cdot \omega_\theta$ can be computed as a function of (ρ_ψ, λ) (being $\omega_\phi = \frac{v_\parallel(E, \lambda)}{R}$, $\omega_\theta = \frac{v_\parallel(E, \lambda)}{R \cdot q}$), and it is shown in figure 9. The yellow bands represent where Ω is minimized at different p. It can be seen that, for both energies (exciting the two modes), the resonances are maximized at around $\rho_\psi = 0.6$ and $\rho_\psi = 0.8$ for $\lambda < -0.5$ with $p = 2, 3$. A sample of the initial fast ion phase-space for shot #73116 has been computed by NUBEAM and it is shown as black dots. The fast particles initial phase space overlaps with the yellow bands, confirming the resonance condition can be fulfilled by the injected particles.

The effects of the anomalous fast ion transport on their distribution function has been analysed with the ad-hoc additional transport model implemented in TRANSP/NUBEAM. The additional transport is modelled as a constant diffusion factor (A) of $2\,\mathrm{m}^2\,\mathrm{s}^{-1}$ for energies above 24 keV, mimicking the expected radial transport induced by the destabilized TAEs. For such fast particle distribution functions, the derivative in
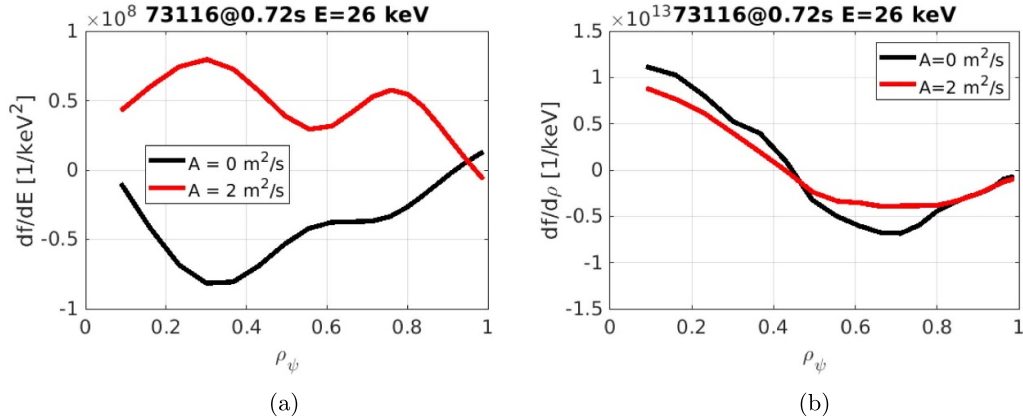
Figure 10. Derivatives of the fast ion distribution function at $E= 26\,keV$ without (black) and with (red) an additional diffusion coefficient. (*a*) Derivative with respect to energy (*b*) derivative with respect to the radial coordinate.
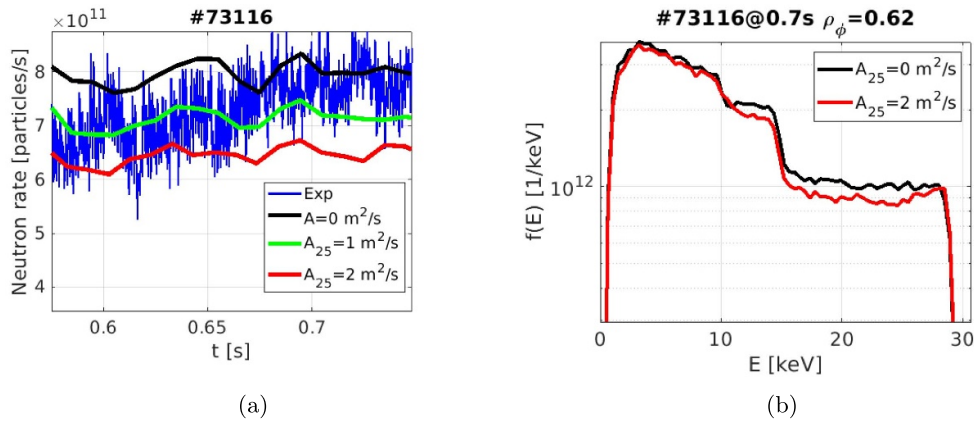

Figure 11. (*a*) Comparison of the experimental neutron rate (blue) and the neutron rate modelled by NUBEAM with different additional diffusion values. $A = 0\,m^2\,s^{-1}$ (black), $A = 1\,m^2\,s^{-1}$ (green), which produces a 10% reduction in the modelled neutron rate, $A = 2\,m^2\,s^{-1}$ (red), which produces a 20% reduction in the neutron rate (*b*) distribution function in energy phase-space at $\rho_\psi = 0.62$ for two different diffusion $A = 0\,m^2\,s^{-1}$ (black), $A = 2\,m^2\,s^{-1}$ (red).

energy and ρ_ψ at $E= 26\,keV$ are computed and illustrated in figure 10. This energy is chosen because the fast particles at this energy are driving the inner TAE mode, and it would be the region of interest for this gradients. In figure 10(*a*), it can be observed that the implemented anomalous diffusion makes the derivative in energy change sign up to roughly $\rho_\psi = 0.9$. The most relevant modification is the change in the derivative in the radial direction (figure 10(*b*)). Indeed, the gradient is reduced (in amplitude) around the location where the $m = (2, 3)$ TAE is excited, i.e. $\rho_\psi \sim 0.6$, as expected due to the fast-ion radial transport outwards and the subsequent flattening of the distribution function. We remark that this transport is only dependent on the energy, and not on the radius. Still the expected flattening of the distribution function is observed.

Further indications on the consistency of the additional fast-ion transport induced by the TAEs can be obtained comparing the neutron rates from the various simulations of TRANSP/NUBEAM with the experimentally measured one (figure 11(*a*)). Indeed, analysing the simulations with (green

and red curves) and without (black curve) anomalous transport, the drop in the neutron rate induced by the TAEs is captured in all the various cases, having the experimental upper values reproduced with only neoclassical transport (black) and the experimental lower values reproduced with the additional transport (red). The additional fast ion transport reduces the energetic particle population in the core. Being the neutrons produced by beam-target reactions, the reduction of the high-energy tail of the particles makes the neutron rate drop significantly. A value between $1\,m^2\,s^{-1}$ and $2\,m^2\,s^{-1}$ qualitatively reproduces the neutron rate trend. A value of $1\,m^2\,s^{-1}$ reduces the neutron rate by 10% and a value of $2\,m^2\,s^{-1}$ by 20%, values close to the result shown in figure 4(*b*) (larger than 10%). Further models accounting for transport dependence in phase-space can give more accurate results, but activity is left for future work. Eventually, the energy distribution of the fast ions at $\rho_\psi = 0.62$ is shown in figure 11(*b*). In the case of additional diffusion (red case in figure), a bump-on tail can be observed, and this could explain the presence of the $n = 0$ mode. In this

case the presence of the bump-on tail is imposed because of TRANSP additional diffusion model.

6. Conclusion

In this work, the identification of TAEs at different radial locations in TCV counter-current NBI scenarios has been presented. The unstable modes feature Alfvènic specific characteristics: they are present only with energetic particles and their frequency increases with the toroidal field, i.e. the Alfvèn frequency. Two modes, with an intermittent behaviour, are observed at the maximum injected energy (26 keV).

The linear MHD stability have been computed with the LIGKA code. Two unstable modes at frequencies consistent with the experimental observations have been detected by LIGKA (and MISHKA) and identified as two different TAEs with toroidal mode number $n = 1$ and poloidal mode numbers $m = (2, 3)$. The T_e fluctuations measured with ECE diagnostic allow to reconstruct the mode structure, which is shown to be in good agreement with the LIGKA computation. A sensitivity scan in $q0$ shows that modification of such value within 10% still produces sensible results. This uncertainty on the q profile could be solved by using measurements for the poloidal magnetic field, like the Imaging Motional Stark Effect diagnostic. ECE allows, for future work, to estimate the mode amplitude and to further validate the modelling results.

In addition, the mutual interaction between NBI fast ions and TAEs is studied by means of TRANSP/NUBEAM. It is shown that the fast ion population filled by the NB is resonant with the observed modes. A sensitivity on the additional ad-hoc diffusion coefficient has been carried out with TRANSP/NUBEAM. The neutron rate drop is recovered on average using a diffusion coefficient of $A = 2\,m^2\,s^{-1}$, for energies $E \geqslant 24\,keV$. Such diffusion coefficient modifies the gradients of the distribution function, reducing them where the $(1, 2)$ TAE is present. From preliminary analyses, moreover, it is suggested that the $(1, 2)$ mode expels fast ions towards larger radii, repopulating thus outer regions of the plasma edge. This firstly results in a reduction of the neutron rates, and in a decrease of the drive for the $(1, 2)$ TAE. Also, the increased fast ion density in the outer regions induces the excitation of the $(1, 3)$ TAE.

Future extensions to this study will include the computation of the fast ions additional transport with the so-called kick-model [23, 24] using the estimated mode structure (scaled with the ECE measurement), and measuring the fast ion transport using FIDA [6] and FILD [3] diagnostics.

Acknowledgments

ORCID iDs

M. Vallar ⬤ https://orcid.org/0000-0002-1792-6702
M. Garcia-Munoz ⬤ https://orcid.org/0000-0002-3241-502X
S. Sharapov ⬤ https://orcid.org/0000-0001-7006-4876

References

[1] Cheng C.Z., Chen L. and Chance M.S. 1985 High-*n* ideal and resistive shear Alfvén waves in tokamaks *Ann. Phys., NY* **161** 21–47
[2] Cheng C.Z. and Chance M.S. 1986 Low-*n* shear Alfvén spectra in axisymmetric toroidal plasmas *Phys. Fluids* **29** 3695–701
[3] Reimerdes H. *et al* (The EUROfusion MST1 Team) 2022 Overview of the TCV tokamak experimental programme *Nucl. Fusion* **62** 042018
[4] Vallar M. *et al* (TCV Team and EUROfusion MST1 Team) 2019 Status, scientific results and technical improvements of the NBH on TCV tokamak *Fusion Eng. Des.* **146** 773–7
[5] Geiger B. *et al* (The ASDEX Upgrade Team) 2014 Fast-ion transport in the presence of magnetic reconnection induced by sawtooth oscillations in ASDEX upgrade *Nucl. Fusion* **54** 022005
[6] Geiger B., Karpushov A., Duval B., Marini C., Sauter O., Andrebe Y., Testa D., Marascheck M., Salewski M. and Schneider P. (The TCV Team and The EUROfusion MST1 Team) 2017 Fast-ion transport in low density l-mode plasmas at TCV using FIDA spectroscopy and the TRANSP code *Plasma Phys. Control. Fusion* **59** 115002
[7] Vallar M. *et al* (The TCV Team) 2022 Modelling of sawtooth-induced fast ion transport in positive and negative triangularity in TCV *Nucl. Fusion* **62** 026028
[8] Cabrera P.A., Labit B., Coda S. and Porte L. (The TCV Team) 2021 High resolution density pedestal measurements during edge localized modes by short-pulse reflectometry in the TCV tokamak *Plasma Phys. Control. Fusion* **63** 085019
[9] Coda S. *et al* (The TCV Team) 2021 Enhanced confinement in diverted negative-triangularity l-mode plasmas in TCV *Plasma Phys. Control. Fusion* **64** 014004
[10] Sharapov S. *et al* (The AUG Team and The EUROfusion MST1 Team) 2017 The effects of electron cyclotron heating and current drive on toroidal Alfvén eigenmodes in tokamak plasmas *Plasma Phys. Control. Fusion* **60** 014026
[11] Kim J. *et al* 2022 Suppression of toroidal Alfvén eigenmodes by the electron cyclotron current drive in KSTAR plasmas *Nucl. Fusion* **62** 026029
[12] Karpushov A.N. *et al* 2017 Neutral beam heating on the TCV tokamak *Fusion Eng. Des.* **123** 468–72
[13] Karpushov A.N. *et al* (The TCV Team) 2022 Upgrade of the neutral beam heating system on the TCV tokamak—second high energy neutral beam *Fusion Eng. Des.* **187** 113384
[14] Testa D., Corne A., Farine G., Jacq C., Maeder T. and Toussaint M. 2015 3D, LTCC-type, high-frequency magnetic sensors for the TCV tokamak *Fusion Eng. Des.* **96** 989–92
[15] Testa D. *et al* The EUROfusion MST1 team and The TCV team 2019 LTCC magnetic sensors at EPFL and TCV: lessons learnt for ITER *Fusion Eng. Des.* **146** 1553–8
[16] Geiger B. *et al* (The TCV and EUROfusion MST1 Teams) 2020 Observation of Alfvén eigenmodes driven by off-axis

neutral beam injection in the TCV tokamak *Plasma Phys. Control. Fusion* **62** 095017

[17] Lauber P., Günter S., Könies A. and Pinches S.D. 2007 Ligka: a linear gyrokinetic code for the description of background kinetic and fast particle effects on the MHD stability in tokamaks *J. Comput. Phys.* **226** 447–65

[18] Mikhailovskii A., Huysmans G., Kerner W. and Sharapov S. 1997 Optimization of computational MHD normal-mode analysis for tokamaks *Plasma Phys. Rep.* **23** 844–57

[19] Tataronis J. and Grossmann W. 1973 Decay of MHD waves by phase mixing *Z. Phys.* A **261** 203–16

[20] Fontana M., Porte L. and Molina Cabrera P. 2017 Correlation electron cyclotron emission diagnostic in TCV *Rev. Sci. Instrum.* **88** 083506

[21] Lin-Liu Y., Chan V. and Prater R. 2003 Electron cyclotron current drive efficiency in general tokamak geometry *Phys. Plasmas* **10** 4064–71

[22] Heidbrink W. 2008 Basic physics of Alfvén instabilities driven by energetic particles in toroidally confined plasmas *Phys. Plasmas* **15** 055501

[23] Podesta M., Gorelenkova M. and White R. 2014 A reduced fast ion transport model for the tokamak transport code TRANSP *Plasma Phys. Control. Fusion* **56** 055003

[24] Podestà M., Gorelenkova M., Gorelenkov N. and White R. 2017 Computation of Alfvèn eigenmode stability and saturation through a reduced fast ion transport model in the TRANSP tokamak transport code *Plasma Phys. Control. Fusion* **59** 095008